Cai *et al.*
Chinese Journal of Mechanical Engineering (2021) 34:128
https://doi.org/10.1186/s10033-021-00654-4

Chinese Journal of Mechanical Engineering

ORIGINAL ARTICLE Open Access

Numerical Study on Effect of Non-uniform CMAS Penetration on TGO Growth and Interface Stress Behavior of APS TBCs

Zhenwei Cai[1,2], Zifan Zhang[1,2], Yingzheng Liu[1,2], Xiaofeng Zhao[3] and Weizhe Wang[1,2*]

Abstract

The penetration of CaO–MgO–Al_2O_3–SiO_2 (CMAS) is one of the most significant factors that induce the failure of air-plasma-sprayed thermal barrier coatings (APS TBCs). The direct penetration of CMAS changes the thermal/mechanical properties of the top coat (TC) layer, which affects the thermal mismatch stress behavior and the growth of thermally grown oxide (TGO) at the TC/bond coat (BC) interface, thereby resulting in a more complicated interface stress state. In the present study, a two-dimensional global model of APS TBCs with half of the TC layer penetrated by CMAS is established to investigate the effect of non-uniform CMAS penetration on the interface stress behavior. Subsequently, a local model extracted from the global model is established to investigate the effects of interface morphologies and CMAS penetration depth. The results show that non-uniform CMAS penetration causes non-uniform TGO growth in APS TBCs, which consequently causes the stress behavior to vary along the interface. Furthermore, the CMAS penetration depth imposes a significant effect on the TC/TGO interface stress behavior, whereas the interface roughness exerts a prominent effect on the stress level at the BC/TGO interface under CMAS penetration. This study reveals the mechanism associated with the effect of non-uniform CMAS penetration on the interface stress behavior in APS TBCSs.

Keywords: CMAS non-uniform penetration, TGO growth, Interface stress, CMAS penetration depth, Interface roughness

1 Introduction

Air plasma sprayed thermal barrier coatings (APS TBCs) are widely used in gas turbines as a critical thermal insulation component [1]. Currently, the penetration of environmental CaO–MgO–Al_2O_3–SiO_2 (CMAS) is one of the most significant factors that induce the failure of air-plasma-sprayed thermal barrier coatings (APS TBCs) [2–4]. The penetration of CMAS into the porous microstructures of the ceramic top coat (TC) of APS TBCs can cause substantial surface modification. First, the change in the mechanical parameters pertaining to the TC layer results in a considerable thermal mismatch stress at the TC/metallic bond coat (BC) interface. Second, the change in the thermal parameter weakens the thermal insulation ability of TBCs, thereby further accelerating the growth of the thermally grown oxide (TGO), and then aggravating the stress state at the TC/BC interface or initiating interface cracks prematurely [5]. Hence, understanding the CMAS penetration effect on the TGO growth and interface stress behavior of APS TBCs is crucial.

The CMAS-penetration-induced surface modification of TBCs has been extensively investigated both experimentally and theoretically. Owing to the considerable difference in material properties between CMAS and the TC material, a CMAS-infiltrated TC layer exhibits thermal/mechanical behaviors that differ completely from that of a TC layer without CMAS penetration [6]. Siddharth

*Correspondence: wangwz0214@sjtu.edu.cn
[1] Key Laboratory of Power Machinery and Engineering, School of Mechanical Engineering, Shanghai Jiao Tong University, Shanghai 200240, China
Full list of author information is available at the end of the article

et al. [7] performed micro-hardness measurement to obtain the mechanical properties of APS TBCs after CMAS penetration and discovered a significant improvement in terms of the Young's modulus, in addition to a decrease in the strain tolerance of TBCs. Kakuda et al. [8] experimentally revealed that the penetration of CMAS resulted in an approximately two-fold increase in thermal conductivity in the TC layer, which further resulted in an increase in temperature at the TC/BC interface, thereby accelerating the growth of TGO or initiating interface cracks, as shown in Figure 1(a) [2, 9, 10]. In some experiments, premature spalling was observed from an interface in APS TBCs under CMAS penetration, as shown in Figure 1(b) [5]. However, the microstructure characteristics of APS TBCs, such as porosity, size, shape, and distribution, primarily depends on the spraying process, which causes the experimentally measured material properties of CMAS-penetrated APS TBCs to vary among different samples. Therefore, simplified theoretical models have been applied to consider the effect of CMAS penetration on the thermal/mechanical properties of TBCs, and the results indicated consistency with experimental results [11–14]. However, the mechanism of CMAS penetration-induced TGO growth and the interface stress behavior in APS TBCs are yet to be elucidated. Hence, some numerical studies have been performed to investigate the CMAS penetration effect on the stress behavior at the TC/BC interface. Shen [15] and Zhou [16] investigated the dynamic TGO growth and the corresponding interface stress behavior in APS TBCs without CMAS penetration; they reported that the interface roughness and TGO non-uniform growth significantly affected the interface stress distribution. When considering the effect of CMAS penetration, Zhang et al. [17] discovered that the CMAS penetration depth affected the interface stress behavior of TBCs because the depth of CMAS penetration determines the modified area in TBCs; however, they disregarded the effects of the interface roughness and TGO growth, which are the most important factors that induce interface cracks [18–21]. Su et al. [22] discovered that CMAS penetration-induced TGO growth increased the Young's modulus in the TC layer and accelerated the initiation and propagation of cracks on the rough interface of TBCs; however, they disregarded the effect of thermal property change on TGO growth. To solve this problem, Xu et al. [23] developed a chemo-thermo-mechanically constitutive theory to describe CMAS corrosion in TBCs. However, the experiments and numerical studies

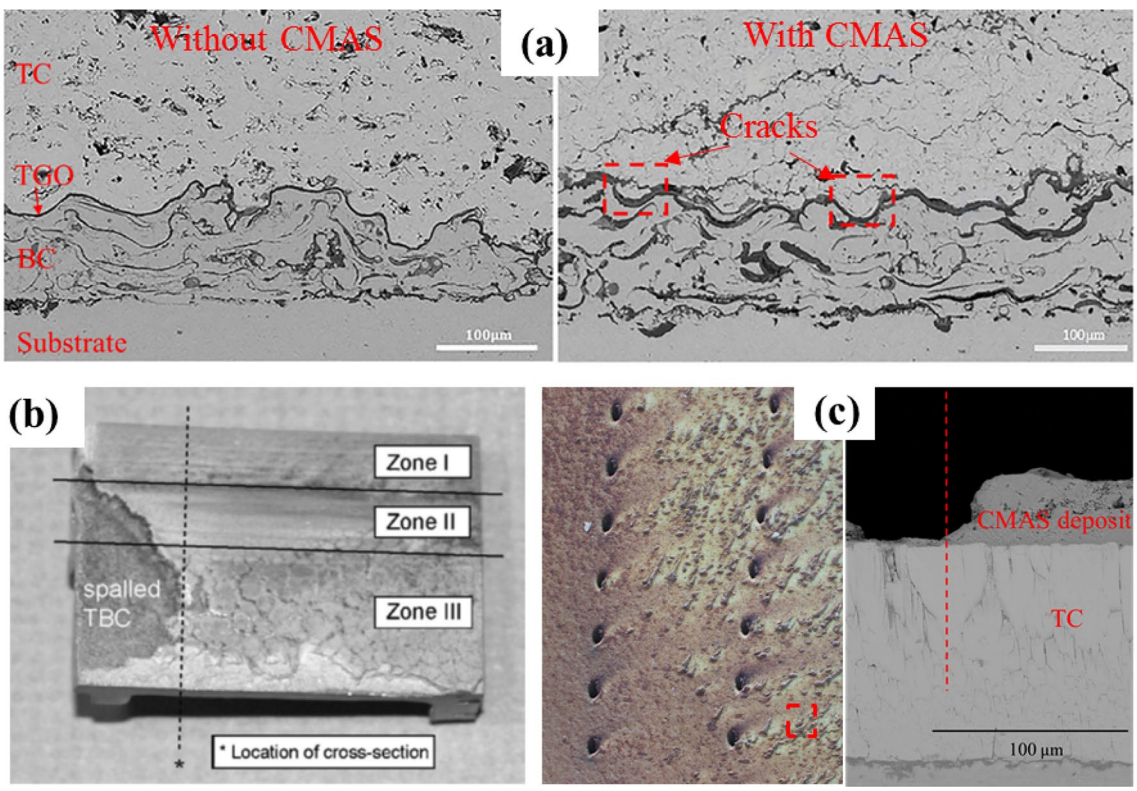

Figure 1 (**a**) Cross-section of APS TBCs without/with CMAS penetration, (**b**) Plan-view optical image showing turbine shroud segment with peeling of TBCs, (**c**) Cross-section image of non-uniform CMAS deposit distribution around partition line

were performed in an isothermal environment, and the temperature gradient in the TBCs and its change with the CMAS penetration depths were not discussed, although TGO growth is extremely sensitive to temperature. In addition, some experiment results showed a non-uniform distribution of CMAS deposits on the blade surface (shown in Figure 1(c)), which might further cause non-uniform CMAS penetration in TBCs or local peeling. Results regarding the effect of CMAS non-uniform penetration on TGO growth and interface stress behavior are scarce. To better understand the abovementioned effect, investigations regarding the CMAS penetration effect on the TGO growth and interface stress behavior of APS TBCs must be performed.

In this study, the effect of CMAS penetration on the TGO growth and stress behavior at the TC/BC interface was investigated numerically. A two-dimensional global model of APS TBCs with half of the TC layer penetrated by CMAS was established to investigate the effect of non-uniform CMAS penetration. In this model, the change in the thermal/mechanical properties induced by CMAS penetration was appropriately considered by the theoretical models, and its effect on the temperature gradient and the dynamic TGO growth in TBCs were investigated. A local model extracted from the global model was used to investigate the effect of interface morphologies and CMAS penetration depth. To simplify the irregular interface morphology in TBCs, the morphology was assumed to be a perfect sinusoid.

2 Numerical Model

2.1 Theoretical Basis of Surface Modification

The CMAS-penetrated TC layer can be regarded as a two-phase composite material. Hence, the effective medium theory can be applied to evaluate the thermal/mechanical properties of TBCs after CMAS penetration. Subsequently, the calculation results can be compared with experimental results reported in the literatures. Before applying the theory, the following are assumed: (1) The CMAS deposit can completely fill each pore in the TC layer; (2) because the reaction effects between the TC material and CMAS are not considered, the phase transformation of the TC material during the cooling stage is negligible; (3) the TC materials are isotropic before and after CMAS infiltration.

2.1.1 Young's Modulus

The mechanical properties of two-phase composite materials depend on the concentration, shape, continuity, and spatial distribution of each phase [24]. Currently, two models (the Voigt model and Reuss model) are used extensively to describe the mechanical properties of composite materials comprising two elastic isotropic components [25, 26]. Between them, the Voigt model assumes that the load causes an equal strain in two phases, and that the stress of the composite material is the sum of the stresses afforded by each phase. Therefore, the Young's modulus of the ceramic layer penetrated by CMAS can be written as the weighted average Young's modulus of the volume fraction for each phase, as follows:

$$E_f = E_c V_c + E_t V_t, \tag{1}$$

where the subscript c represents CMAS, t the TC material, and f the material parameters of the TC layer after CMAS infiltration. E_c and E_t are the Young's moduli of CMAS and TC material (bulk), respectively; V_c and V_t are the volume fractions of CMAS and the TC layer, respectively. Generally, the porosity of the ceramic layer is 10%; therefore, $V_c = 0.1$ and $V_t = 0.9$.

The Reuss model assumes that the stress in two phases in the composite are equal; hence, the total strain of the composite is equal to the sum of the strains in each phase. Therefore, the Young's modulus of the TC layer penetrated by CMAS can be expressed as

$$E_f = \left(\frac{V_c}{E_c} + \frac{V_t}{E_t} \right)^{-1}, \tag{2}$$

Comparing the results calculated using the two abovementioned models with the experimental results, it was discovered that the Reuss model afforded a higher accuracy [24, 27]. Therefore, the Reuss model was used in the present study to calculate the Young's modulus of a CMAS-penetrated TC layer. In addition, it is generally believed the effect of CMAS penetration on the Poisson's ratio of the TC material is minimal [24].

2.1.2 Thermal Expansion Coefficient

The thermal expansion coefficient of the TC layer after CMAS penetration can be described using the Schapery model, as follows [28]:

$$\alpha_f = \frac{\alpha_c E_c V_c + \alpha_t E_t V_t}{E_c V_c + E_t V_t}, \tag{3}$$

where α_c and α_t are the thermal expansion coefficients of CMAS and the TC material, respectively.

As presented, the thermal expansion coefficient of the TC layer after CMAS penetration is correlated with the porosity in the TC layer and the thermal expansion coefficient of CMAS. Studies showed that the penetration of CMAS with different compositions resulted in a 5%–15% decrease in the thermal expansion coefficient for TBCs with a porosity of 0.1 [24]. In the present study, the thermal expansion coefficient of the TC layer reduced by 6.2% after CMAS penetration (as calculated

using Eq. (3)), which agrees wells with the range provided in the abovementioned study.

2.1.3 Thermal Conductivity

The microstructure characteristics of APS TBCs are extremely complex; in fact, the size, shape, and distribution of the microstructures significantly affect the thermal conductivity of the coatings. The relationship between the microstructure characteristics and thermal conductivity of APS TBCs has been investigated extensively [27, 29–32]. To obtain the thermal conductivity of APS TBCs after CMAS penetration, two theoretical methods are typically used: the Maxwell model [13] and the Rayleigh model [14]. Between them, the Maxwell model assumes that the microstructures in the TC layer are spherical and not in contact with each other. Therefore, the thermal conductivity of a TC layer penetrated by CMAS is expressed as

$$k_f = k_t \left[1 + 3V_c \left(\frac{\gamma + 2}{\gamma - 2} - V_c \right)^{-1} \right], \tag{4}$$

where k_c and k_t are the thermal conductivity of CMAS and the TC material, respectively. $\gamma = k_c/k_t$ is the ratio of thermal conductivity in CMAS and the TC material.

The Rayleigh model can be written as

$$k_f = k_t[1 + V_c(\gamma - 1_c)]. \tag{5}$$

In a previous study [8], the Maxwell and Rayleigh models were used to calculate the thermal conductivity of the TC layer after CMAS penetration, and the results indicated a reduction by 10% and 2%, respectively, as compared with before CMAS penetration. This shows that the Rayleigh model affords a better calculation accuracy. Therefore, the Rayleigh model was used in the present study to calculate the thermal conductivity of a CMAS-penetrated TC layer.

2.1.4 Specific Heat

Generally, the specific heat of the TC layer after CMAS penetration is associated with the specific heat, volume fraction, and density of each phases, and it can be written as:

$$C_f = C_t\omega_t + C_c\omega_c, \tag{6}$$

where C_t and C_c are the specific heat of the TC material and CMAS, respectively; ω_t and ω_c are the mass fractions of the TC material and CMAS, respectively, which can be written as

$$\omega_i = \frac{V_i\rho_i}{\sum_{j=1}^{2} V_i\rho_i}, \tag{7}$$

where ρ_i is the density of each phase. The specific heat calculated using Eq. (6) differed from the experimental results by 4% [8], indicating that the model can be used to calculate the specific heat of the CMAS-penetrated TC layer with reasonable accurately.

2.1.5 Density

By disregarding the phase change of the TC material in the present study, the density of the CMAS-penetrated TC layer can be calculated as follows [8]:

$$\rho_f = V_t\rho_t + V_c\rho_c. \tag{8}$$

It is noteworthy that the TC material used in the equation above is the bulk material, which differs from the material where microstructures are considered in the TC layer.

2.2 FEM Model and Boundary Conditions

2.2.1 Global Model

Figure 2(a) shows a two-dimensional multi-period global model of APS TBCs with CMAS non-uniform penetration. Here, multi-period implies that the model is

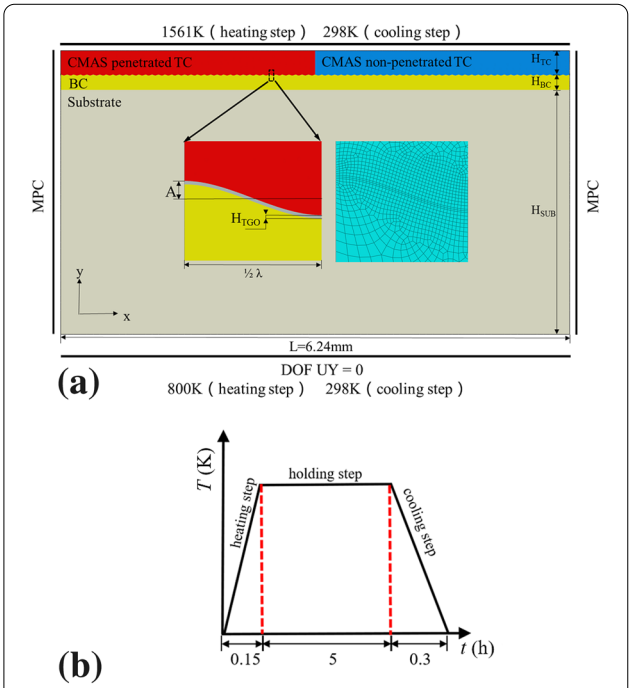

Figure 2 (**a**) Two-dimensional multi-period global model of APS TBCs with CMAS non-uniform penetration, (**b**) thermal boundary conditions of model

sufficiently long in the x-axis to allow the consideration of more interface morphologies. In the model, the thickness of the TC layer H_{TC} was 300 μm, the thickness of the BC layer H_{BC} was 180 μm, the thickness of the substrate H_{SUB} was 3 mm, and the initial thickness of the TGO layer H_{TGO} was 1 μm. The dynamic growth of TGO was considered in the simulation. To consider the effect of the interface roughness in the APS TBCs, the interface morphology in the model was simplified to a perfect sinusoid [18, 19]. The sinusoidal curve is expressed as $y(x) = A \cdot \sin(2\pi x/\lambda)$; therefore, the roughness of the interface is controlled by the amplitude A and the wavelength λ, which are obtained by observing the cross-sectional morphology in experiments [33]. In this study, λ was set to a constant value of 80 μm, and amplitude A was set to between 5 and 20 μm, as shown in Figure 2(a). Base on the size of the CMAS non-uniform coverage area on the blade surface shown in Figure 1(c), the length of the global model L was set to 6.24 mm, which contained 78 sinusoidal periods at the TC/TGO/BC interface. The effect of CMAS penetration was considered based on the thermal/mechanical change of the TC layer. Previous studies have demonstrated that CMAS exerts the greatest effect on the interface stress behavior when it penetrates the bottom of the TC layer [24]. Therefore, to investigate the effect of non-uniform CMAS penetration, the left-half TC layer in the model was completely penetrated by CMAS, i.e., the penetration depth $H_{CP} = H_{TC} = 300$ μm, whereas the right-half was not penetrated by CMAS. Because the APS TBCs model was assumed to be part of the blade, the left and right boundaries of the model was set as a multi-point constraint to ensure that all points at the boundaries can propagate simultaneously in the x-direction. The bottom boundary of the model was constrained in the y-direction, whereas the upper surface boundary was unconstrained. The heat flux on the left and right boundary was 0 (adiabatic).

The element type used in the model was 4-node plane strain thermally coupled quadrilateral, bilinear displacement and temperature (CPE4T). Refined meshes were applied in the region around the TGO layer to improve the stress estimation accuracy therein. To investigate the effect of CMAS penetration on the temperature distribution in the TBCs, the thermal cycle condition was determined [34]. As shown in Figure 2(b), the initial temperature of the model was 298 K. During heating, the temperature at the upper surface increased to 1561 K linearly within 0.15 h, whereas the temperature at the lower surface increased to 800 K. The dwell time was 5 h. Subsequently, the temperature at the upper and lower surfaces decreased to 298 K during cooling (0.3 h). A finite element analysis was conducted using the commercial software ABAQUS 6.13 [35].

2.2.2 Local Model

To further investigate the effects of CMAS penetration depth and interface roughness on the interface stress behavior in the APS TBCs under non-uniform CMAS penetration, a critical zone was selected to perform a local modeling based on the results from the multi-period global model. As shown in Figure 3, the critical Zone II was located around the partition line of CMAS in the multi-period model. To observe the TGO growth behavior caused by the local non-uniform CMAS penetration around the partition line, Zone II was imposed with a two-period length ($2L$): the left period involved CMAS penetration, whereas the right period did not. The constraints and thermal boundary conditions of the local model was consistent with the multi-period model. The effects of different CMAS penetration depths ($H_{CP} = 0$, 100, 200, and 300 μm) on the TGO growth and interface stress behavior were investigated. The effects of different interface roughness levels under CMAS penetration are discussed herein.

2.2.3 Material Parameters

In the present study, the material used for the TC was ZrO_2-8wt.% Y_2O_3 (8YSZ), whereas that used for the BC was NiCoCrAlY. The material used for the substrate was Hastelloy-X. The TC layer was assumed to as visco-elastic, whereas the other layers were visco-plastic. For the APS TBCs without CMAS penetration, the fundamental material properties of each layer are shown in Table 1. The CMAS penetration only

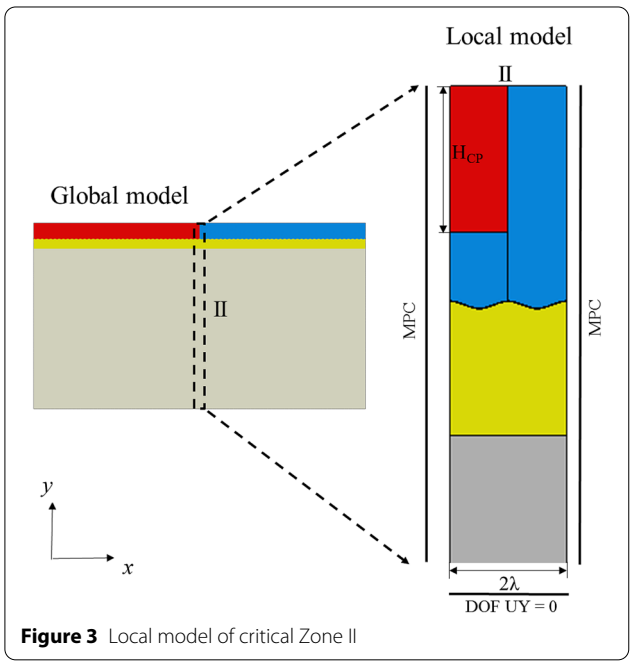

Figure 3 Local model of critical Zone II

Table 1 Material properties for all layers of APS TBCs [37–41]

	T (°C)	*E* (GPa)	*v*	*a* (/10^6K)	*k* (W/mK)	*C* (J/kg·K)	*ρ* (kg/m^3)
TC	25	17.5	0.2	9.68	1.05	483	5650
	800			9.88			
	1000	12.4		10.34			
TGO	25	380	0.27	5.1	25.2	857	3978
	800	338					
	1000	312		9.8			
BC	25	220	0.3	10.3	4.3	501	7320
	400	200		12.7	6.4	592	
	800	164		14.1	10.2	781	
	1000	120		20.4	11.1	764	
SUB	100	209	0.38	11.1	11.4	544	8110
	300	199	0.38	13.3	14.9		
	500	185	0.39	14.0	18.3		
	700	167	0.39	14.6	21.8		
	900	145	0.40	15.4	25.2		
	1100	123	0.40	17.3	28.7		

Table 2 Material properties of CMAS-penetrated TC layer [42]

T (℃)	*E* (GPa)	*v*	*a* (/10^6 K)	*k* (W/mK)	*C* (J/kg·K)	*ρ* (kg/m^3)
25	19	0.2	8.57	2.09	501	5339
1000	12.4		10.34			

changed the material properties of the TC layer. As shown in Table 2, the thermal/mechanical properties of the CMAS-penetrated TC layer were calculated using Eqs. (1)–(8), and the results agreed well with the range of material change of previous studies [8, 24, 27]. As shown in Table 2, the elastic modulus, equivalent thermal conductivity, and specific heat capacity of the TC layer increased after CMAS infiltration. In particular, the thermal conductivity increased by approximately twice, whereas the equivalent density and the equivalent thermal expansion coefficient decreased. The creep behavior of all of the layers can be described by the Norton equation $\dot{\varepsilon}_{cr} = B\sigma^n$, where $\dot{\varepsilon}_{cr}$ and σ are the creep strain rate and stress respectively, whereas B and n are material properties. The corresponding creep parameters of each layer are listed in Table 3.

Table 3 Creep parameters of different layers in APS TBCs [42]

Layer	*B* ($s^{-1}MPa^{-1}$)	*n*
TC	1.8×10^{-11}–1.8×10^{-5}	1
BC	2.15×10^{-8}	2.45
SUB	7.54×10^{-28}	4.78

Table 4 Parameters for TGO growth model [43]

n	*R* (J/mol·K)	*C* (μm/$s^{0.25}$)	*Q* (J/mol)
0.25	8.314472	748	87575

2.2.4 TGO Growth Model

The TGO layer will grow at high temperatures. Its growth rate is associated with temperature and time. The thickness of the TGO layer can be written as Eq. (9) [36].

$$h_{TGO} = C \cdot \exp\left(-\frac{Q}{R \cdot T}\right) t^n, \tag{9}$$

where, h_{TGO} is the thickness of the TGO layer; R is the universal gas constant; T is the temperature; t is the time; n is the BC layer oxidation exponent; C and Q are fitting parameters. These parameters are shown in Table 4.

The TGO growth process can be approximated as expansion along the thickness direction, and its expansion (growth) strain can be written as

$$\varepsilon_{\mathrm{TGO}} = \ln\frac{h_{TGO}}{h_0}, \tag{10}$$

where h_0 is the initial thickness of the TGO, which is generally set as 1 μm.

Therefore, the TGO growth rate can be written as

$$\dot{\varepsilon}_{\mathrm{TGO}} = \frac{\mathrm{d}\varepsilon_{\mathrm{TGO}}}{\mathrm{d}t} = \frac{nk_p t^{n-1}}{k_p t^n + h_0}. \tag{11}$$

Furthermore,

$$\dot{\varepsilon}_{TGO}(0) = 0. \tag{12}$$

It can be deduced that the TGO growth rate $\dot{\varepsilon}_{TGO}$ decreases with time. In the ABAQUS software, the TGO growth can be simulated by defining the anisotropic swelling of the material.

3 Results and Discussion

3.1 TGO Growth and Interface Stress Behavior in APS TBCs Under Non-uniform CMAS Penetration

Figure 4(a) shows the temperature distribution of the multi-period model of the APS TBCs under non-uniform CMAS penetration. It is evident that the temperature distributions were different between the areas with and without CMAS penetration. In the left-half model, CMAS penetration deteriorated the thermal insulation performance in the area therein. Therefore, the temperature in the left-half model was significantly higher than that in the right-half model. This induced a transverse (x-direction) heat flow from the left to the right region in the model. Temperature gradients appeared in both the transverse and thickness directions, which is a more complicated situation than that without CMAS non-uniform penetration. To further investigate the temperature distribution in different areas of the model, three paths along the thickness direction were selected: Path 1(the left side of the model), Path 2 (the left side of the model), and Path 3 ((the right side of the model), as shown in Figure 4(a). Figure 4(b) shows the temperature distortion along the three paths. The temperature gradient of the TC layer along Path 1 was much smaller than that along Path 3. This indicates that CMAS penetration will impose a greater effect on the temperature distribution at the interface. The temperature gradient of the TC layer along Path 2 was that between Path 1 and Path 3, indicating that the non-uniform CMAS penetration caused a temperature change in the transverse direction, which will further affect TGO growth.

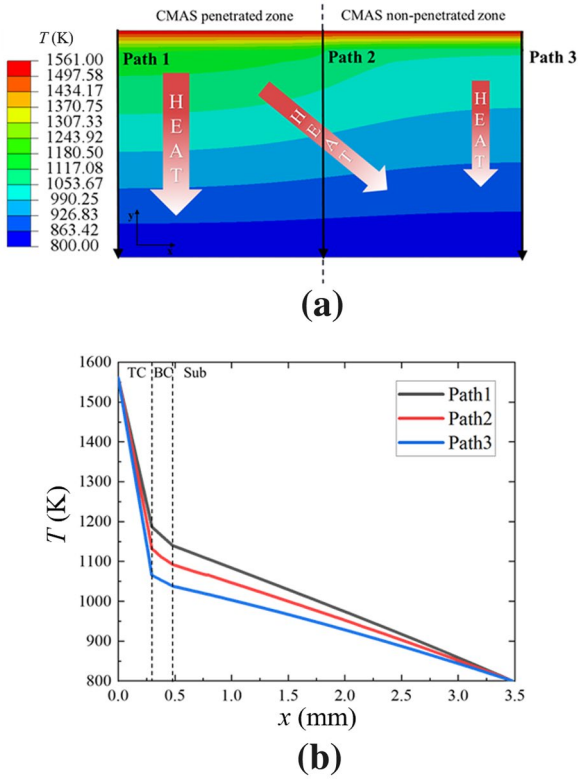

Figure 4 (**a**) Temperature distribution of multi-period global model of APS TBCs under non-uniform CMAS penetration, (**b**) temperature distributions along three paths in model

For a clearer analysis, two critical zones (Zones I and III) were selected, as shown in Figure 5(a). Owing to the significant length of the multi-period global model, the CMAS penetration in Zone I is approximately uniform (H_{CP} = 300 μm), whereas Zone III can be regarded as not being affected by CMAS penetration (H_{CP} = 0 μm). Figure 5(b) shows the temperature distribution at the interface of the multi-period model after heating was performed. It is evident that the temperature at the interface of the CMAS-penetrated half-model was much higher than that of the CMAS-non-penetrated right-half model. The maximum temperature difference at the interface from the left and right sides of the model can reach 120 K, and areas closer to the partition line indicated a greater traverse temperature gradient. In addition, the temperature distribution showed slight fluctuations along the interface, which were caused by the interface roughness. Figure 5(c) shows the interface temperature distribution in three critical zones: I, II, and III. Among them, the interface temperature curve in Zones I and III were relatively gentle. Meanwhile, the transverse temperature difference in Zone II reached 22 K, which might cause non-uniform TGO growth therein. Additionally, the

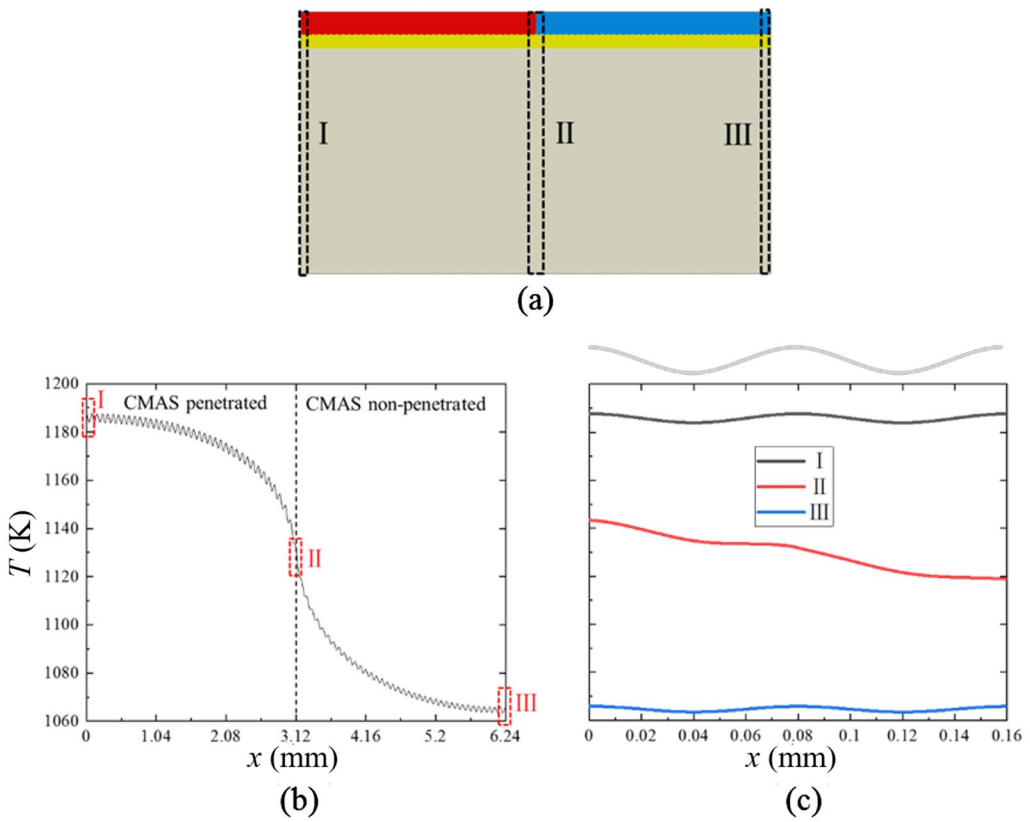

Figure 5 (**a**) Critical zones: I, II and III, (**b**) temperature distribution at interface of multi-period model after heating, (**c**) interface temperature distribution in three critical zones: I, II, and III

interface roughness causes a non-uniform TGO growth at the peak and valley locations in one interface period. These effects resulted in a more complex TGO growth behavior in Zone II, thereby affecting the interface stress behavior therein.

Figure 6(a) shows the distribution of TGO thickness in the multi-period global model. Consistent with the temperature distribution shown in Figure 5(a), the TGO thickness in the CMAS-penetrated side of the APS TBCs can reach 2.18 μm, which is significantly higher than that in the non-penetrated side (1.45 μm). In addition, as shown in Figure 6(b), the TGO thickness in Zone I was greater than that in Zone III, which might result in different interface stress behaviors in the two regions. Although the TGO thickness in Zone II was smaller than that in Zone I, the transverse temperature difference around the partition line caused the left-side TGO thickness to be greater than that at the right side. This non-uniform TGO growth behavior around the partition line of CMAS will further affect the interface stress behavior therein—this will be discussed next.

Generally, the initiation of interface cracks primarily depends on the interface tensile stress in the thickness direction (y-axis), i.e., σ_{22}, where σ_{22} increases gradually and reaches its maximum at the end of cooling. Therefore, only σ_{22} at the end of cooling was obtained and analyzed in this study. Figure 7 shows the σ_{22} distribution in the TC and BC layers of the multi-period global model of the APS TBCs at room temperature. As shown, σ_{22} was concentrated in the valley locations around the interface of the TC layer, and the stress state at the peak positions was compressive. Comparing the stress distributions in the three critical zones of the TC layer, it was discovered that σ_{22} was proportional to the TGO thickness therein (shown in Figure 6(b)); therefore, σ_{22} in Zone I is the highest, followed by that at Zones II and III. The maximum σ_{22} values in Zones I and III were 317 and 110 MPa, respectively. The non-uniform TGO growth around the partition line in Zone II resulted in a stress difference between the left and right sides, and the maximum stress difference was 40 MPa. Contrary to the stress distribution in the TC layer, the σ_{22} in the BC layer primarily concentrated at the peak locations around the interface, and the stress state at the valley locations was compressive. The stress level in the BC layer was significantly lower than that in

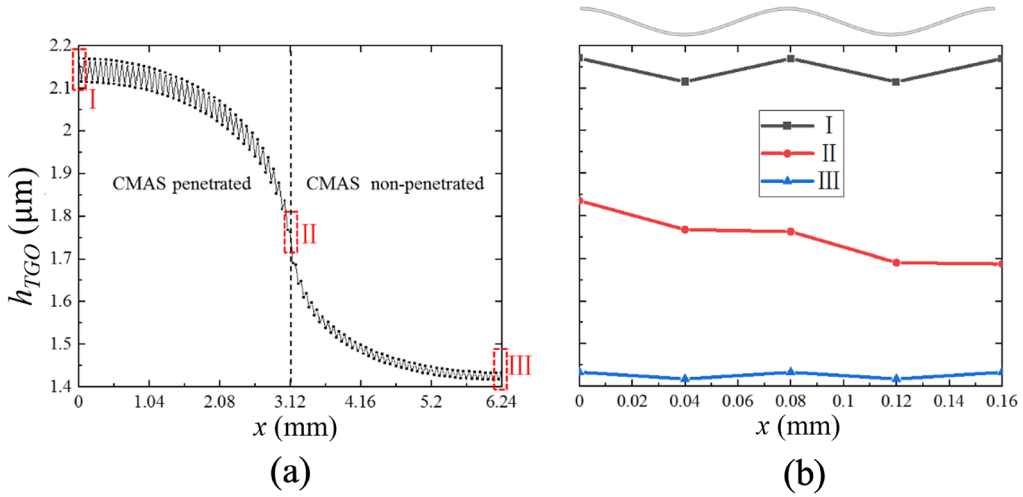

Figure 6 (**a**) Distribution of TGO thickness in multi-period global model of APS TBCs, (**b**) distribution of TGO thickness in three critical zones: I, II, and III

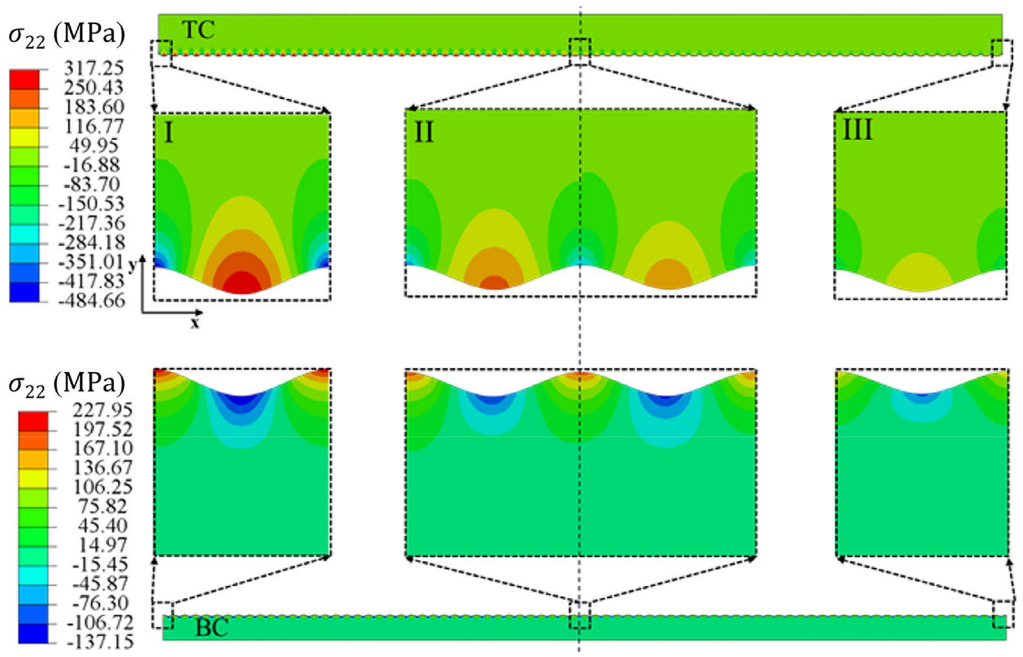

Figure 7 Distribution of σ_{22} in TC and BC layers of multi-period global model of APS TBCs at room temperature

the TC layer, and the stress difference between the left and right sides in Zone II was evident in the BC layer. The results above indicate that the non-uniform CMAS penetration in the APS TBCs will result in a non-uniform interface stress distribution at the interface, and that the σ_{22} at the interface of the CMAS-penetrated area was much larger than that in the non-penetrated area.

Figure 8 shows the σ_{22} distribution at the TC/TGO and BC/TGO interfaces of the multi-period global model of the APS TBCs under non-uniform CMAS penetration. The different stress states at the peaks or valleys in the

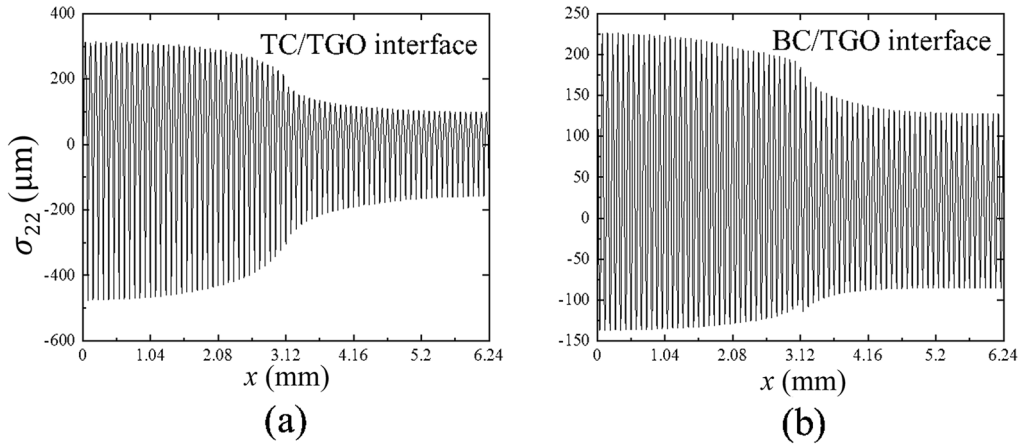

Figure 8 Distribution of σ_{22} at (**a**) TC/TGO, and (**b**) BC/TGO interface of multi-period global model of APS TBCs

one-period interface shows that the interface roughness significantly affected the interface stress distribution. Furthermore, the stress difference between the peak and valley at the left-side interface was much larger than that at the right-side interface, indicating that CMAS penetration aggravated the stress difference induced by the interface roughness. In addition, it was observed that the CMAS penetration effects on the stress level at the TC/TGO and BC/TGO interfaces were different. Figure 9 shows the σ_{22} distribution at the interface in the three critical zones. As shown in Figure 9(a), the σ_{22} at the valleys of the TC/TGO interface increased from 98 MPa (Zone III) to 317 MPa (Zone I) with CMAS penetration. In Zone II, a significant stress difference was observed at the two peak locations around the partition line. As shown in Figure 9(b), the stress state at the BC/TGO interface was opposite to that at the TC/TGO interface. The σ_{22} at the of peaks the BC/TGO interface increased from 125 MPa (Zone III) to 228 MPa (Zone I). Comparing the stress distribution at the two interfaces, it was discovered that CMAS penetration imposed a greater effect on the σ_{22} at the TC/TGO interface. To summarize, at the TC/TGO and BC/TGO interfaces, CMAS penetration might accelerate crack initiation at the valleys and peaks, respectively.

3.2 Effect of CMAS Penetration Depth

Figure 10(a) shows the temperature distribution at the interface of Zone II under different CMAS penetration depths (H_{CP} = 0 100, 200, 300 μm). The results were obtained based on the local model of Zone II (shown in Figure 3). The interface temperature distribution at the

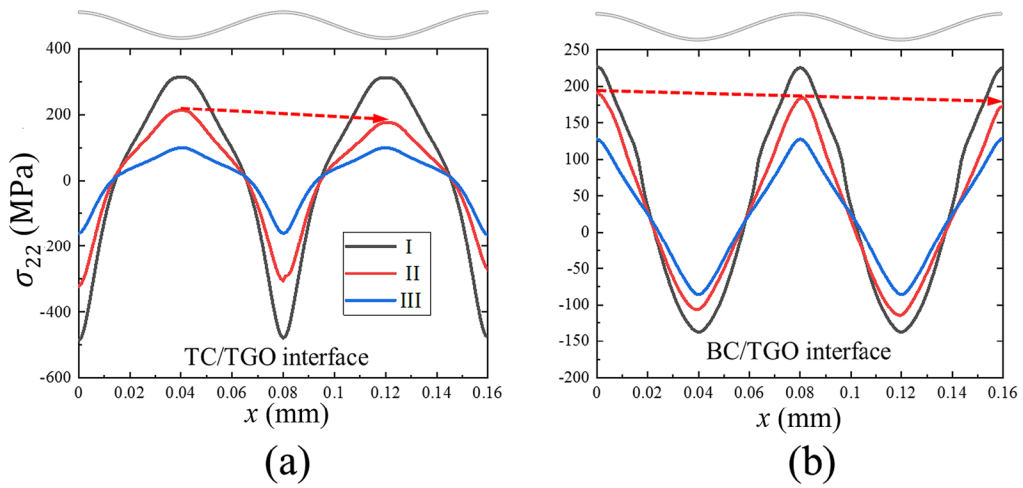

Figure 9 Distribution of σ_{22} at (**a**) TC/TGO, and (**b**) BC/TGO of three critical zones

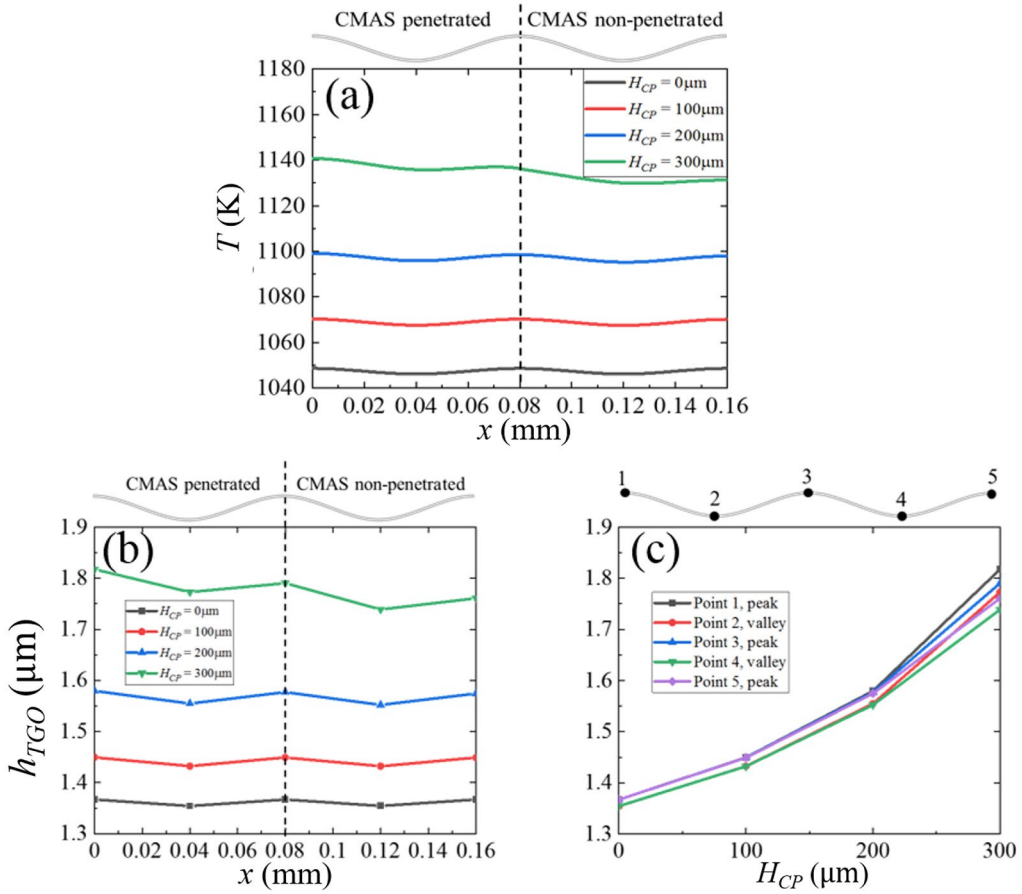

Figure 10 (**a**) Temperature distribution at interface of Zone II under different CMAS penetration depths (H_{CP} = 0, 100, 200, and 300 μm), (**b**) distribution of TGO thickness under different CMAS penetration depths, (**c**) TGO thickness at peaks and valleys of interface under different CMAS penetration depths

two sides of the interface was completely symmetrical for the case without CMAS penetration (H_{CP} = 0 μm). As the CMAS penetration depth increased, the interface temperature increased gradually owing to the thermal conductivity change in the CMAS-penetrated region of the TC layer. When the left region of TC layer was completely penetrated by CMAS (H_{CP} = 300 μm), the temperature at the left-side interface increased by 90 K (x = 0 mm) compared with the case without CMAS penetration. In addition, the temperature difference between the left and right sides around the partition line increased with the CMAS penetration depth. To further investigate effect of temperature difference on the TGO growth behavior, the distribution of TGO thickness under different CMAS penetration depths is presented in Figure 10(b). Consistent with the temperature distribution shown in Figure 10(a), the TGO layer increased gradually with the CMAS penetration depth. Figure 10(c) shows the TGO thickness at the peaks and valleys of the interface under different CMAS penetration depths. As shown, the difference in the TGO thickness between the left and right sides around the partition line increased with the CMAS penetration depth. This indicates that CMAS penetration accelerated the non-uniform TGO growth around the partition line, which might further affect the interface stress behavior.

Figure 11 shows the σ_{22} distribution in the TC and BC layers of Zone II under different CMAS penetration depths. Similar to the stress distribution at the interface of the multi-period model, a stress difference was observed around the partition line. As the CMAS penetration depth increased, the tensile stress in both the TC and BC layers increase considerably, and the maximum stress appeared at the interface. Figure 12 shows the σ_{22} distribution at the TC/TGO and BC/TGO interfaces under different CMAS penetration depths. As shown, when the CMAS penetration depth increased, the σ_{22} difference around the partition line increased. In addition,

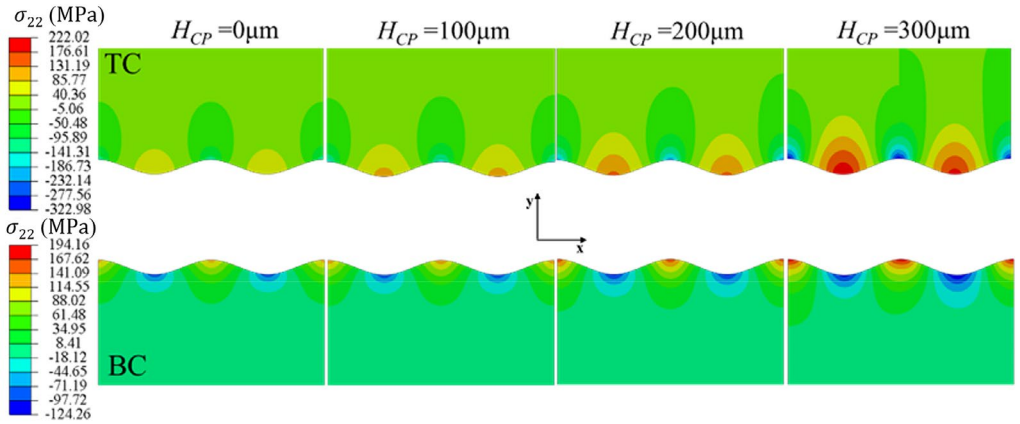

Figure 11 Distribution of σ_{22} in TC and BC layers of Zone II under different CMAS penetration depths

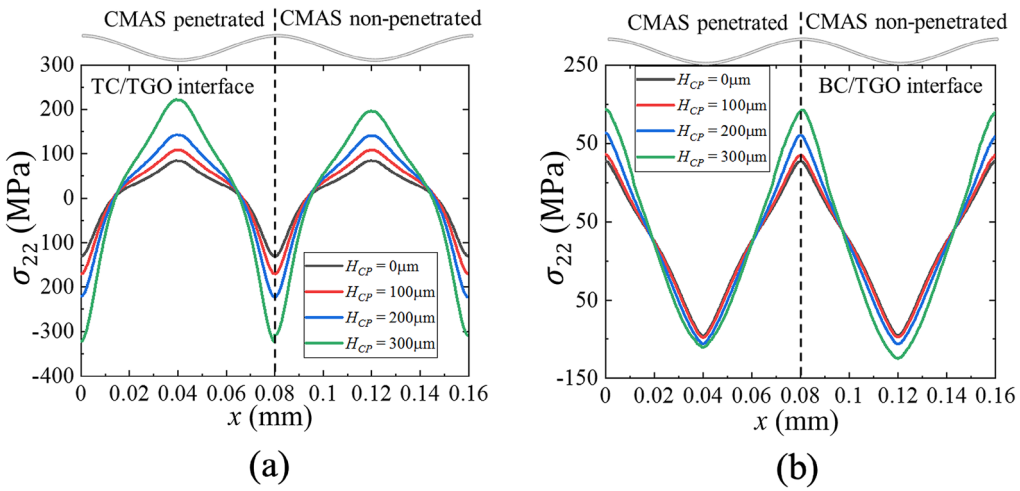

Figure 12 Distribution of σ_{22} at (**a**) TC/TGO, and (**b**) BC/TGO interfaces under different CMAS penetration depths

the CMAS penetration depth affected the stress behavior at the two interfaces differently. When the TC layer was completely penetrated by CMAS, the stress difference around the partition line at the valleys of the TC/TGO interface reached 30 MPa, whereas that at the peaks of BC/TGO interface was approximately 0 MPa. This shows that the CMAS penetration depth imposed a greater effect on the TC/TGO interface stress behavior and might accelerate crack initiation at the valleys of the TC/TGO interface at the CMAS-penetrated side.

3.3 Effect of Interface Roughness

Figure 13(a) and (b) shows the interface temperature distribution of Zone II under different interface amplitudes (A = 5, 10, and 2 μm). The calculation for all cases was based on H_{CP} = 300 μm. The interface temperature distribution was asymmetrical around the partition line of the left side, and this asymmetrical phenomenon became more evident as A increased. As A increased from 5 to 20 μm, the temperature at the peak (point 1) increased by 12 K, whereas the temperature at the peak of the right side (point 5) only increased by 8 K, as shown in Figure 13(c). This shows that CMAS penetration aggravated the effect of interface roughness on the temperature at the peaks of the interface. The temperature at the valleys exhibited different trends depending on A: the temperature at the valley of the left side of the interface decreased (Point 2), whereas that of the right side of the interface increased slightly (Point 4). This is due to the heat conduction from the adjacent peaks with high temperature in the TGO.

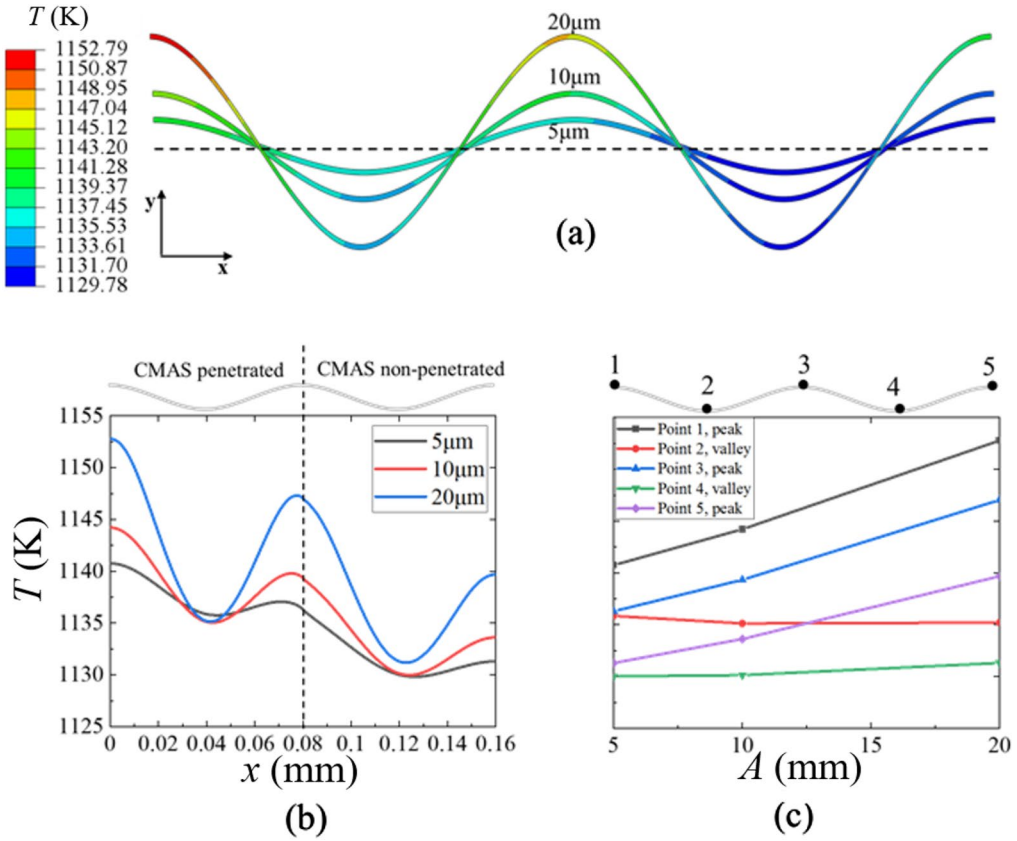

Figure 13 (**a**) Temperature contour of TGO in Zone II under different interface amplitudes (A = 5, 10, and 20 μm), (**b**) interface temperature distribution of Zone II under different interface amplitudes, (**c**) temperature at peaks and valleys of interface under different interface amplitudes

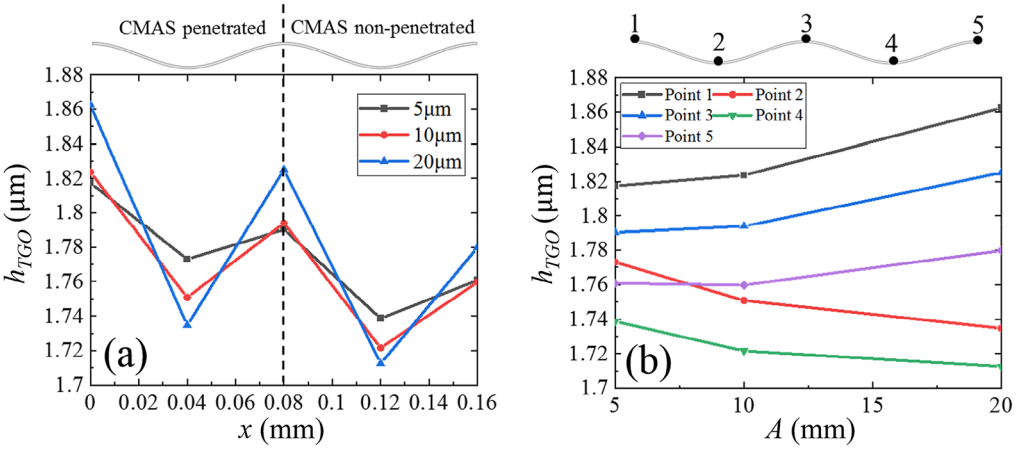

Figure 14 (**a**) Distribution of TGO thickness for different interface amplitudes, (**b**) TGO thickness at peaks and valleys of interface vs. interface amplitude

Figure 14(a) shows the distribution of TGO thickness for different interface amplitudes. Similar to the interface temperature distribution shown in Figure 13, the maximum TGO thickness appeared at the peak of the left side (Point 1), whereas the minimum appeared at the valley of the right side (Point 4). When A increased from 5

to 10 μm, the TGO thickness increased slightly, whereas it increased significantly when A increased to 20 μm, as shown in Figure 14(b). This shows that the TGO growth was not proportional to A.

To investigate the effect of TGO thickness on the interface stress behavior, the σ_{22} distribution in the TC and BC layers of Zone II under different values of A is presented, as shown in Figure 15. For the TC layer, the interface stress redistributed as A increased, whereas the position with the maximum σ_{22} shifted gradually from the valley to both sides of the valley (off-valley). For the BC layer, as A increased, the σ_{22} at the peaks increased significantly from 200 to 630 MPa, whereas the position with the maximum σ_{22} did not change. Figure 16 shows the σ_{22} distribution at the TC/TGO and BC/TGO interfaces of Zone II under different interface roughness values. It is evident that the stress redistribution at the TC/TGO interface and the maximum σ_{22} value increased slightly. The stress difference around the partition line induced by the non-uniform CMAS penetration increased slightly at the TC/TGO interface. Compared with the stress level at the TC/TGO interface, the maximum σ_{22} at the BC/TGO interface increased considerably, and the stress distribution fluctuated slightly when A increased to 20 μm. To summarize, the interface roughness changed the stress distribution at the TC/TGO interface; however, it exerted a more significant effect on the stress level at the BC/TGO interface under CMAS penetration.

4 Conclusions

The effect of CMAS penetration on the TGO growth and stress behavior at the TC/BC interface was investigated numerically in this study. First, the change in thermal/mechanical properties induced by CMAS

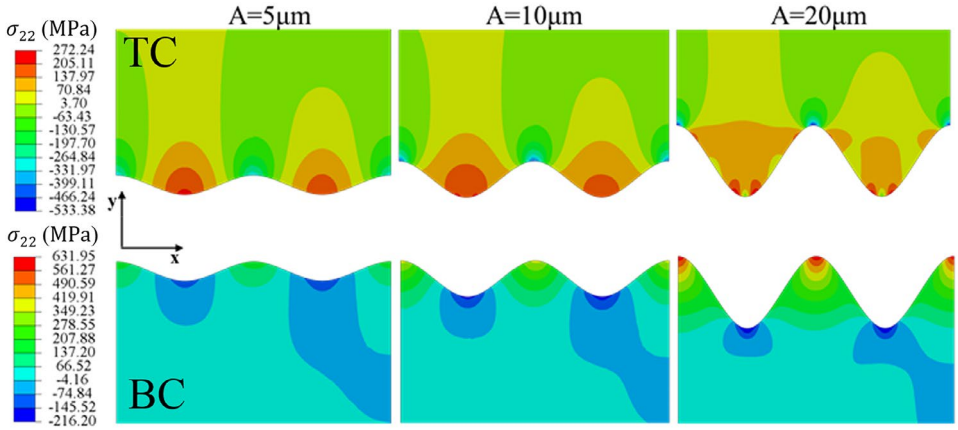

Figure 15 Distribution of σ_{22} in TC and BC layers of Zone II under different interface amplitudes

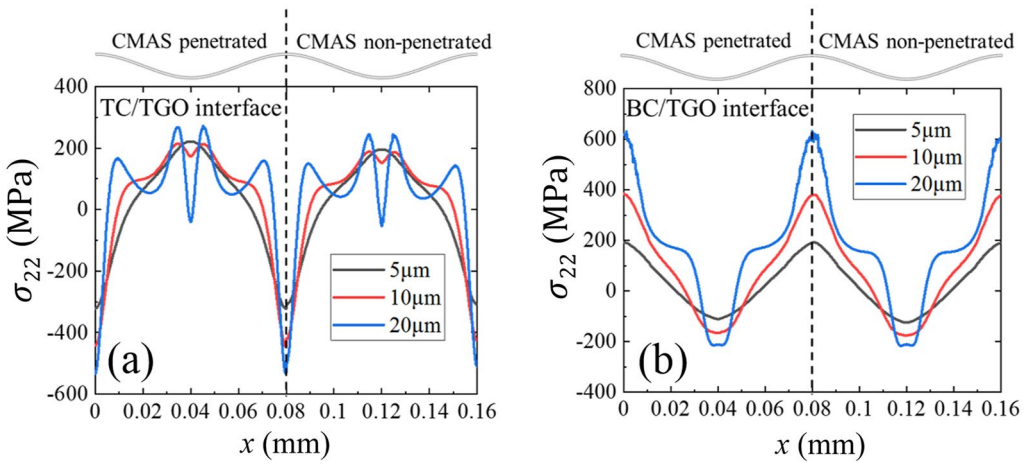

Figure 16 Distribution of σ_{22} at TC/TGO and BC/TGO interfaces of Zone II under different interface roughness values

penetration was considered using theoretical models. The effect of non-uniform CMAS penetration was investigated using a two-dimensional global model of APS TBCs, where half of the TC was penetrated by CMAS. The effects of interface roughness and CMAS penetration depth were discussed based on a local model. The conclusions were as follows:

(1) CMAS penetration deteriorated the thermal insulation performance of the CMAS penetration area of the APS TBCs, which then resulted in a temperature difference of approximately 100 K between the penetrated and non-penetrated areas. Temperature gradients were present in both the transverse and thickness directions.
(2) Non-uniform CMAS penetration in the APS TBCs caused a non-uniform TGO growth, which resulted in a more complicated interface stress distribution. At the TC/TGO and BC/TGO interfaces, CMAS penetration might accelerate crack initiation at the valleys and peaks, respectively.
(3) When the CMAS penetration depth increased, the difference in σ_{22} around the partition line of CMAS increased. The CMAS penetration depth affected the stress behavior at the TC/TGO and BC/TGO interfaces differently. The CMAS penetration depth imposed a greater effect on the TC/TGO interface stress behavior and might accelerate crack initiation at the valleys of the TC/TGO interface at the CMAS-penetrated side.
(4) Compared with the TC/TGO interface, the maximum σ_{22} at the BC/TGO interface increased considerably. The interface roughness changed the stress distribution at the TC/TGO interface but imposed a more prominent effect on the stress level at the BC/TGO interface under CMAS penetration.

Acknowledgments
Not applicable.

Authors' contributions
WW was in charge of the whole trial; ZC wrote the manuscript; ZC and ZZ performed the numerical calculations. YL was assisted with the edition of the manuscript; XZ provided the experiment results. All authors read and approved the final manuscript.

Authors' Information
Zhenwei Cai, born in 1992, is a postdoctor at *Key Laboratory of Power Machinery and Engineering, School of Mechanical Engineering, Shanghai Jiao Tong University*, *China*. His research interests include the strength evaluation of high-temperature structural components and the intelligent manufacturing of advanced thermal barrier coatings.
Zifan Zhang, born in 1996, is currently a master candidate at *Key Laboratory of Power Machinery and Engineering, School of Mechanical Engineering, Shanghai Jiao Tong University*, *China*. His research interests include the strength evaluation of thermal barrier coatings.
Yingzheng Liu, born in 1972, is currently a professor at *Key Laboratory of Power Machinery and Engineering, School of Mechanical Engineering*, *Shanghai Jiao Tong University*. He is the director of *Gas Turbine Research Institute of Shanghai Jiao Tong University*.
Xiaofeng Zhao, is currently a professor at *School of Materials Science and Engineering, Shanghai Jiao Tong University*, *China*. His research interests include high-temperature coatings, such as thermal barrier coatings used in aero engines and gas turbines, anti-corrosion coatings for nuclear reactor fuel claddings, and other anti-oxidation and wear-resistant coatings.
Weizhe Wang, born in 1977, is currently a professor at *School of Materials Science and Engineering, Shanghai Jiao Tong University*, *China*. He mainly focuses on the major national demand industries (aviation, ground gas turbines, smart energy), and conducts research on digital twin technology of process systems and component systems.

Funding
Supported by the National Natural Science Foundation of China (Grant No. 51875341).

Competing Interests
The authors declare no competing financial interests.

Author Details
[1]Key Laboratory of Power Machinery and Engineering, School of Mechanical Engineering, Shanghai Jiao Tong University, Shanghai 200240, China. [2]Gas Turbine Research Institute, Shanghai Jiao Tong University, Shanghai 200240, China. [3]School of Materials Science and Engineering, Shanghai Jiao Tong University, Shanghai 200240, China.

Received: 3 January 2021 Revised: 3 October 2021 Accepted: 14 November 2021
Published online: 04 December 2021

References

[1] K W Schlichting, N P Padture, E H Jordan, et al. Failure modes in plasma-sprayed thermal barrier coatings. *Materials Science & Engineering A (Structural Materials: Properties, Microstructure and Processing)*, 2003, 342(1–2): 120–130.
[2] W R Chen, L R Zhao. Review: Volcanic ash and its influence on aircraft engine components. *Procedia Engineering*, 2015, 99: 795–803.
[3] Z W Cai, J S Jiang, W Z Wang, et al. CMAS penetration-induced cracking behavior in the ceramic top coat of APS TBCs. *Ceramics International*, 2019, 45(11): 14366–14375.
[4] Z W Cai, H Hong, W Z Wang, et al. Stress evolution in ceramic top coat of air plasma-sprayed thermal barrier coatings due to CMAS penetration under thermal cycle loading. *Surface and Coatings Technology*, 2019, 381: 125146.
[5] S Krämer, S Faulhaber, M Chambers, et al. Mechanisms of cracking and delamination within thick thermal barrier systems in aero-engines subject to calcium-magnesium-alumino-silicate (CMAS) penetration. *Materials Science & Engineering A*, 2008, 490(1): 26–35.
[6] A R Krause, H F Garces, G Dwivedi, et al. Calcia-magnesia-alumino-silicate (CMAS)-induced degradation and failure of air plasma sprayed yttria-stabilized zirconia thermal barrier coatings. *Acta Materialia*, 2016, 105: 355–366.
[7] S Lokachari S, W Song, J Yuan, et al. Influence of molten volcanic ash infiltration on the friability of APS thermal barrier coatings. *Ceramics International*, 2020, 46(8): 11364–11371.
[8] T R Kakuda, C G Levi, T D Bennett. The thermal behavior of CMAS-infiltrated thermal barrier coatings. *Surface and Coatings Technology*, 2015, 272: 350–356.
[9] R Darolia. Thermal barrier coatings technology: Critical review, progress update, remaining challenges and prospects. *International Materials Reviews*, 2013, 58(6): 315–348.
[10] Y Wu, H Luo, C Cai, et al. Comparison of CMAS corrosion and sintering induced microstructural characteristics of APS thermal barrier coatings. *Journal of Materials Science & Technology*, 2019, 35(3): 440–447.

[11] T Nakamura, T Wang, S Sampath. Determination of properties of graded materials by inverse analysis and instrumented indentation. *Acta Materialia*, 2000, 48(17): 4293–4306.
[12] L Su, X Chen, T J Wang. Numerical analysis of CMAS penetration induced interfacial delamination of transversely isotropic ceramic coat in thermal barrier coating system. *Surface & Coatings Technology*, 2015, 250: 100–109.
[13] J C A Maxwell. A Treatise on Electricity and Magnetism. *Nature*, 7(182): 478–480.
[14] J W Rayleigh. On the influence of obstacles arranged in rectangular order upon the properties of a medium. *Philosophical Magazine*, 1892, 34(211): 481–502.
[15] Q Shen, L Yang, Y C Zhou, et al. Effects of growth stress in finite–deformation thermally grown oxide on failure mechanism of thermal barrier coatings. *Mechanics of Materials*, 2017, 114: 228–242.
[16] Q Zhou, L Yang, C Luo, et al. Thermal barrier coatings failure mechanism during the interfacial oxidation process under the interaction between interface by cohesive zone model and brittle fracture by phase-field. *International Journal of Solids and Structures*, 2021, s 214–215: 18–34.
[17] G Zhang, X Fan, R Xu, et al. Transient thermal stress due to the penetration of calcium-magnesium-alumino-silicate in EB-PVD thermal barrier coating system. *Ceramics International*, 2018: S0272884218309362.
[18] K Yuan, Y Yu, J F Wen. A study on the thermal cyclic behavior of thermal barrier coatings with different MCrAlY roughness. *Vacuum*, 2017, 137: 72–80.
[19] Q M Yu, H L Zhou, L B Wang. Influences of interface morphology and thermally grown oxide thickness on residual stress distribution in thermal barrier coating system. *Ceramics International*, 2016, 42(7): 8338–8350.
[20] K Si, A Jones, M A E Jepson, et al. Effects of three-dimensional coating interfaces on thermo-mechanical stresses within plasma spray thermal barrier coatings. *Materials & Design*, 2017, 125: 189–204.
[21] D E Mack, T Wobst, M O D Jarligo, et al. Lifetime and failure modes of plasma sprayed thermal barrier coatings in thermal gradient rig tests with simultaneous CMAS injection. *Surface and Coatings Technology*, 2017: S0257897217304474.
[22] L Su, C Yi. Effects of CMAS penetration on the delamination cracks in EB-PVD thermal barrier coatings with curved interface. *Ceramics International*, 2017: 8893–8897.
[23] G Xu, L Yang, Y C Zhou, et al. A chemo-thermo-mechanically constitutive theory for thermal barrier coatings under CMAS infiltration and corrosion. *Journal of the Mechanics and Physics of Solids*, 2019, 133: 103710.
[24] R W Jackson, E M Zaleski, D L Poerschke, et al. Interaction of molten silicates with thermal barrier coatings under temperature gradients. *Acta Materialia*, 2015, 89: 396–407.
[25] Y M Chiang, D P Birnie, W D Kingery. *Physical ceramics*. New York: J. Wiley, 1997.
[26] Z Hashin. On elastic behaviour of fibre reinforced materials of arbitrary transverse phase geometry. *Journal of the Mechanics & Physics of Solids*, 1965, 13(3): 119–134.
[27] J Wu, H B Guo, Y Z Gao, et al. Microstructure and thermo-physical properties of yttria stabilized zirconia coatings with CMAS deposits. *Journal of the European Ceramic Society*, 2011, 31(10): 1881–1888.
[28] R A Schapery. Thermal expansion coefficients of composite materials based on energy principles. *Journal of Composite Materials*, 1968, 2(3): 380–404.
[29] R Kumar, D Cietek, C Jiang, et al. Influence of microstructure on the durability of gadolinium zirconate thermal barrier coatings using APS & SPPS processes. *Surface and Coatings Technology*, 2018, 337: 117–125.
[30] L Cai, W Ma, B Ma, et al. Air plasma-sprayed La2Zr2O7-SrZrO3 composite thermal barrier coating subjected to CaO-MgO-Al_2O_3-SiO_2 (CMAS). *Journal of Thermal Spray Technology*, 2017, 26(5566): 1–8.
[31] Z Wang, A Kulkarni, S Deshpande, et al. Effects of pores and interfaces on effective properties of plasma sprayed zirconia coatings. *Acta Materialia*, 2003, 51(18): 5319–5334.
[32] A Kulkarni, Z Wang, T Nakamura, et al. Comprehensive microstructural characterization and predictive property modeling of plasma-sprayed zirconia coatings. *Acta Materialia*, 2003, 51(9): 2457–2475.
[33] U Schulz, C Leyens, K Fritscher, et al. Some recent trends in research and technology of advanced thermal barrier coatings. *Aerospace Ence and Technology*, 2003, 7(1): 73–80.
[34] W Wang, P Sun, J Ren, et al. Radiative effectiveness on the aero and thermodynamics in a highly thermally loaded film cooling system. *ASME 2011 Turbo Expo: Turbine Technical Conference and Exposition*. 2011: 325–334.
[35] Simulia D C S. *Abaqus 6.11 analysis user's manual*. 2011.
[36] L Su, W Zhang, Y Sun, et al. Effect of TGO creep on top-coat cracking induced by cyclic displacement instability in a thermal barrier coating system. *Surface & Coatings Technology*, 2014, 254: 410–417.
[37] M Ranjbar-Far, J Absi, S Shahidi, et al. Impact of the non–homogenous temperature distribution and the coatings process modeling on the thermal barrier coatings system. *Materials & Design*, 2011, 32(2): 728–735.
[38] K M Kim, S Shin, H L Dong, et al. Influence of material properties on temperature and thermal stress of thermal barrier coating near a normal cooling hole. *International Journal of Heat & Mass Transfer*, 2011, 54(25–26): 5192–5199.
[39] L Wang, Y Wang, X G Sun, et al. Influence of pores on the thermal insulation behavior of thermal barrier coatings prepared by atmospheric plasma spray. *Materials & Design*, 2011, 32(1): 36–47.
[40] E B Zaretsky, G I Kanel, S V Razorenov, et al. Impact strength properties of nickel-based refractory superalloys at normal and elevated temperatures. *International Journal of Impact Engineering*, 2005, 31(1): 41–54.
[41] C J Hyde, T H Hyde, W Sun, et al. Small ring testing of a creep resistant material. *Materials Science & Engineering A Structural Materials Properties Microstructure & Processing*, 2013, 586(6): 358–366.
[42] J S Jiang J, W Z Wang, X F Zhao, et al. Numerical analyses of the residual stress and top coat cracking behavior in thermal barrier coatings under cyclic thermal loading. *Engineering Fracture Mechanics*, 2018, 196: 191–205.
[43] T Beck, R Herzog, O Trunova, et al. Damage mechanisms and lifetime behavior of plasma-sprayed thermal barrier coating systems for gas turbines — Part II: Modeling. *Surface & Coatings Technology*, 2008, 202(24): 5901–5908.